Density dependence of transient electron thermal transport property in LHD

Density dependence of transient electron thermal transport property in LHD

T. Kobayashi[1,2], K. Ida[1], T. Ii Tsujimura[1], S. Inagaki[3,4], T. Tokuzawa[1], H. Tsuchiya[1], N. Tamura[1], H. Igami[1], Y. Yoshimura[1], S.-I. Itoh[4,3,5], K. Itoh[6,1,4] and LHD Experiment Group

[1] National Institute for Fusion Science, National Institutes of Natural Sciences, Toki 509-5292, Japan

[2] SOKENDAI (The Graduate University for Advanced Studies), Toki 509-5292, Japan

[3] Research Institute for Applied Mechanics, Kyushu University, Kasuga 816-8580, Japan

[4] Research Center for Plasma Turbulence, Kyushu University, Kasuga 816-8580, Japan

[5] Graduate School of Engineering, Chubu University, Kasugai 487-8501, Japan

[6] Institute of Science and Technology Research, Chubu University, Kasugai 487-8501, Japan

E-mail: kobayashi.tatsuya@LHD.nifs.ac.jp

Abstract. In this paper, we investigate data from the density scan experiment in order to clarify how the transport hysteresis width depends on the density. As the line averaged density increases, the hysteresis width almost monotonically decreases. To discuss the physical mechanism of the hysteresis formation, a theoretical model describing the direct response of the fluctuation amplitude to the heating is examined. The model predicts that decreasing density enhances the hysteresis width in the turbulent thermal transport, which is not in contradiction with the present observation. It is found that the model tends to estimate the parameter window in which the hysteresis emerges narrower than the experimental observation.

1. Introduction

Transient response of the electron thermal transport in the magnetically confined torus plasmas is one of the long standing unsolved mysteries. It is typically observed when the core plasma is subject to abrupt heating or cooling, including the electron cyclotron resonance heating (ECH) application [1, 2, 3], the heat pulse induced by the sawtooth crush [4, 5], and the edge cooling by the impurity injection [6, 7, 8]. Refer to the recently published overview papers for a comprehensive understanding [9, 10]. Several experimental investigations have revealed that the classical transport model that only uses scalar transport coefficients is not sufficient to describe the transient response of the electron temperature [11, 12, 13]. The electron heat flux immediately responds to the perturbation before the local electron temperature or its gradient changes, which manifests the existence of "hidden parameters" as a variable for the heat flux in addition to these local variables. A theory predicts that the heating power itself can directly impact on the heat flux [14, 15]. This insight is important for the global plasma confinement as well because it is strongly related to how the power degradation of the global confinement scaling occurs.

There are several possible techniques for analyzing the transient electron thermal transport. The most frequently used method would be the model of the electron heat flux with the diffusivity and the pinch velocity. Although this method is useful because transport properties can be represented by two scaler coefficients, transport nature cannot be described correctly in case the model function is not valid. Instead, we

attempt to directly describe the relation between the electron heat flux and the electron temperature gradient to study the transport property. The electron heat flux is obtained using the energy conservation equation. Direct calculation of the electron heat flux allows us to study the transport nature without assuming a specific transport model.

In LHD, investigations for the transient response of the electron thermal transport have been performed using the modulation ECH (MECH) technique [3]. Due to the immediate response of the heat flux to the heating and the continuous change of the local electron temperature gradient, the flux-gradient diagram shows a hysteresis-type trajectory. The hysteresis also appears in the turbulence response on the electron temperature gradient, corresponding to the theoretical predictions [14, 15]. It is found that the width of the hysteresis depends both on the radius and the heating power [3]. The hysteresis width is known to depend on the density empirically, but dedicated experiments have not been performed and how the hysteresis width depends on the density is not completely revealed.

In this paper, we investigate data from the density scan experiment in order to clarify how the hysteresis width depends on the density. As the line averaged density increases, the hysteresis width almost monotonically decreases. To discuss the physical mechanism of the hysteresis formation, a theoretical model describing the direct response of the fluctuation amplitude to the heating [14, 15] is examined. The model predicts that decreasing density enhances the hysteresis width in the turbulent thermal transport, which is not in contradiction with the present observation. It is found that the model

tends to estimate the parameter window in which the hysteresis emerges narrower than the experimental observation, showing the necessity of further model development as well as direct observation of the response in the fluctuation amplitude.

2. Experimental setup

The density scan experiments are performed in the first deuterium plasma campaign in the Large Helical Device (LHD). The confinement magnetic field is mainly generated by the superconducting helical coils with the toroidal period of $n = 10$ and the poloidal period of $m = 2$. Magnetic field strength is set to be $B = 2.7$ T at the magnetic axis of $R_{\rm ax} = 3.6$ m. The plasmas are sustained by two nearly balanced tangential neutral beam injection systems (NBIs) with the total port through power of ~ 4.5 MW. The MECH with the port through power of ~ 0.7 MW is applied to investigate the transient electron thermal transport. The X mode second harmonic heating with the 154 GHz gyrotron is used for the MECH. The modulation waveform is the rectangular wave of the frequency of $f_{\rm MECH} = 23$ Hz. The shot-to-shot density scan is performed by using the precisely controlled gas puff system, in the range of the line averaged density of $0.4 < \bar{n}_{\rm e} < 2.3 \ \times 10^{19}$ m^{-3}. The electron temperature perturbation is diagnosed by the electron cyclotron emission radiometer system (ECE) [16], whose signal intensity is cross-calibrated by the electron temperature profile measured by the Thomson scattering system.

3. Results

3.1. Density scan experiments

Figure 1 shows the time evolution of the line averaged density and of the electron temperature for the lower density discharge (# 138118) and the higher density discharge (# 138135), as well as the MEHC pulse pattern. These two discharges are in the normal confinement regime, as will be discussed below. During the time period that is subject to the transport analysis, the line averaged density remains almost unchanged. Waveforms of the electron temperature perturbation are characterized by the quasi-triangular wave. In the lower density discharge, the amplitude of the electron temperature perturbation is larger compared to that in the higher density discharge.

Figure 2 shows the line averaged density dependence of the mean plasma parameters. As the line averaged density is increased, the central electron density increases while the central electron temperature remains nearly unchanged. As shown by the black dashed curve in Fig. 2 (a), the center of the ECH absorption profile $r_{\mathrm{eff,dep}}$ calculated by the ray-tracing code "LHD Gauss" [17] satisfies $r_{\mathrm{eff,dep}} < 0.1$ m in all the discharges. Shape of the density profile changes from the almost flat profile to the hollow profile. The electron temperature profile is always peaked at the center due to the centrally focused ECH power. As a result, the plasma stored energy by electrons W_{pe} approximately linearly increases. When the electron density is low, the shine through ratio of the NBIs is relatively high so that the NBI power absorption for electrons $P_{\mathrm{NB,e}}$ decreases as the line averaged density decreases. The time averaged ECH absorption

power P_{ECH} depends little on the plasma parameters in the present scan. Note that P_{ECH} is almost the half of the port through power because of the nearly 50 % duty cycle of the modulation waveform. A proxy of the electron energy confinement time, $W_{\mathrm{pe}}/P_{\mathrm{e}}$, where $P_{\mathrm{e}} = P_{\mathrm{NB,e}} + P_{\mathrm{ECH}}$ is the total heating power absorbed by electrons, increases following the power law on the line averaged density, $W_{\mathrm{pe}}/P_{\mathrm{e}} \propto \bar{n}_e^{0.317}$, shown by the dashed line in Fig. 2 (e).

It has been confirmed that the core electron thermal confinement transits from the normal confinement mode to the internal transport barrier (ITB) mode by decreasing density below a threshold value [18]. Since the target discharges cover a wide density range, it is necessary to analyze the confinement mode of each discharge. In the normal confinement mode, the more degraded the confinement (or the temperature gradient) is the higher the local temperature becomes, following the Bohm-like scaling row. Meanwhile, the confinement of the ITB plasmas surpass the Bohm-like scaling. Therefore, by observing the relation between the electron temperature and its gradient, whether the electron ITB is formed or not can be judged. Figure 3 shows the electron temperature plotted as a function of the electron temperature gradient in $0.12 \leq r_{\mathrm{eff}} \leq 0.35$ m for some representative discharges. Except for cases of very low line averaged density ($\bar{n}_e < 0.6 \times 10^{19}$ m^{-3}), the magnitude of the electron temperature gradient decreases as the electron temperature increases when $T_{\mathrm{e}} > 2.8$ keV, i.e., in the core region side. This tendency corresponds to the typical feature of the normal confinement mode. Low line averaged density cases show the increasing electron

temperature gradient with the increasing electron temperature, being consistent with the electron ITB characteristics. The achieved core electron temperature in these two discharges is slightly higher than the other discharges as shown in Fig. 2 (c), too. The ranges of the line averaged density for the two confinement regimes are labeled in Fig. 2.

3.2. Radial profile of electron temperature response

The electron thermal transport is studied by analyzing the response of the electron temperature to the MECH of $f_{\mathrm{MECH}} = 23$ Hz. Before performing the analysis, high frequency components ($f > 200$ Hz) and the higher harmonic components of the commercial power supply frequency ($m \times 60$ Hz with $m \leq 3$) are removed from the ECE signals. Furthermore, the conditional averaging technique is applied to improve the signal to noise ratio for the transient transport analysis. The conditional averaging for the ECE signal $I_{\mathrm{ECE}}(t)$ is defined as

$$\bar{I}_{\mathrm{ECE}}(\tau) = \frac{1}{N}\sum_{i=1}^{N} I_{\mathrm{ECE}}(t_i + \tau) \tag{1}$$

where $-T/2 < \tau < T/2$ and $T = f_{\mathrm{MECH}}^{-1}$ is the period of the MECH. The value t_i indicates the i-th MECH turn-on time and N is the total number of the modulation.

The procedure of the analysis is demonstrated using two discharges, one having a lower line averaged density (# 138118) and the other a higher line averaged density (# 138135). The electron temperature profiles and their gradient of these two discharges are shown in Fig. 4 (a). The radial profiles of the perturbation amplitude of the electron temperature and the delay time with respect to the MECH pulse pattern are shown in

Fig. 4 (b) and (c), respectively. The ECH absorption profile shown in Fig. 4 (b) indicates that the MECH power is mostly absorbed in the very core region, $r_{\mathrm{eff}} < 0.13$ m. All the observable natures of the electron temperature, including the centrally peaked mean electron temperature, the centrally peaked perturbation amplitude, and the minimal delay at the core, are consistent with the result of the ray-tracing code.

Regarding the heat pulse transport property, two discharges are significantly different. In the higher density case, the slopes of the perturbation amplitude profile and the delay profile are approximately constant with a slight change of the trend at $r_{\mathrm{eff}} \sim 0.35$ m. In the lower density case, the perturbation amplitude profile and the delay profile are relatively flat in $r_{\mathrm{eff}} < 0.25$ m, and the slopes suddenly increase in $0.25 < r_{\mathrm{eff}} < 0.35$ m. Further outside, $0.35 < r_{\mathrm{eff}} < 0.45$ m, the slope of the delay profile becomes weaker again. In general, the smaller slopes in the amplitude and delay profiles correspond to the larger transient transport [19]. Therefore, flattening of the slopes in the core region in the lower density discharge corresponds to a confinement degradation.

This kind of flattening is typically seen when the static magnetic island is formed, too [20]. When the static magnetic island is formed, the mean electron temperature gradient also becomes very small. However, the mean electron temperature gradient in the lower density case is as large as that in the higher density case, in which the slopes of the amplitude profile and the delay profile are finite. Therefore, the flattening observed here is considered to be not due to formation of the static magnetic island.

3.3. Electron heat flux

We analyze electron thermal transport not by assuming a specific transport model but by directly evaluating the electron heat flux $q_{\rm e}$ from the energy conservation equation, following the tradition of the previous study [11]. The energy conservation equation written for $q_{\rm e}$ is given as

$$q_{\rm e}(t, r_{\rm eff}) = \frac{1}{S}\int_0^{r_{\rm eff}} dV \left[P_{\rm ECH}(t, r_{\rm eff}) + P_{\rm NB,e}(r_{\rm eff}) - n_{\rm e}\frac{\partial T_{\rm e}(t, r_{\rm eff})}{\partial t} \right] \tag{2}$$

where $P_{\rm ECH}(t, r_{\rm eff})$ and $P_{\rm NB,e}(r_{\rm eff})$ are the heating power density from the ECH and the NBI, and S and V are the surface area and the volume inside the flux surface labelled by $r_{\rm eff}$. For drawing the flux-gradient relation, the electron temperature gradient is evaluated by the finite subtraction. It should be noted that the estimation error in the ray-tracing calculation provides a significant impact on the evaluated $q_{\rm e}$, and can bring a dummy hysteresis. In the previous study, the hysteresis not only in the heat flux but also in the turbulence amplitude is observed by an independent diagnostic system, proving that the hysteresis in the transport is not a dummy. In the present experiments, there is no turbulence data. Instead, detailed estimation of errors in the ECH antenna direction is performed. It is verified that the following discussion is not due to the estimation error in the ECH absorption profile. Refer to the Appendix.

Figure 5 shows the time evolution of the electron heat flux and the electron temperature gradient. The time label τ corresponds to that in Eq. (1). The values of the heat flux immediately before and after the ECH turn-on and turn-off, i.e., $-0.05 < f_{\rm MECH}\tau < 0.05$, $f_{\rm MECH}\tau < -0.45$ and $0.45 < f_{\rm MECH}\tau$, are not reasonable.

This is because the fast response of the ECE signal is mitigated by the low pass filter aiming for the noise rejection. Therefore, the analysis of the flux-gradient relation below is performed by using the time windows $-0.45 < f_{\mathrm{MECH}}\tau < -0.05$ and $0.05 < f_{\mathrm{MECH}}\tau < 0.45$ [colored by light blue and light green in Fig. 5 (a,b) and (c,d), respectively].

Diagrams of the flux-gradient relation are shown in Fig. 6. When the line averaged density is lower [case (a)], the width of the hysteresis loop, i.e., the distance between the top side line and the bottom side line, is typically larger. The hysteresis width in the plasma core side seems to be larger rather than that in the edge side. To discuss the density dependence in detail, the hysteresis width is quantified by use of the linear fitting for the top side line and the bottom side line. The linear fitting is performed for data in $-0.45 < f_{\mathrm{MECH}}\tau < -0.05$ and $0.05 < f_{\mathrm{MECH}}\tau < 0.45$ shown by the light blue lines in Fig. 6 (a) and by the light green lines in Fig 6 (b), respectively. Fitted lines are shown by the blue lines and by the orange lines, respectively. The changes in the electron temperature gradient in these time windows are different, and are denoted as $[-\nabla T_{\mathrm{e,min}}^{\mathrm{top}}, -\nabla T_{\mathrm{e,max}}^{\mathrm{top}}]$ and $[-\nabla T_{\mathrm{e,min}}^{\mathrm{bottom}}, -\nabla T_{\mathrm{e,max}}^{\mathrm{bottom}}]$, respectively. The distance between the top side line and the bottom side line of the hysteresis loop is evaluated at three points, $-\nabla T_{\mathrm{e,min}} = \max(-\nabla T_{\mathrm{e,min}}^{\mathrm{top}}, -\nabla T_{\mathrm{e,min}}^{\mathrm{bottom}})$, $-\nabla T_{\mathrm{e,max}} = \min(-\nabla T_{\mathrm{e,max}}^{\mathrm{top}}, -\nabla T_{\mathrm{e,max}}^{\mathrm{bottom}})$, and $-\nabla T_{\mathrm{e,center}} = (-\nabla T_{\mathrm{e,max}} - \nabla T_{\mathrm{e,min}})/2$. Symbols in Fig. 6 show the values of the electron heat flux on the linearly fitted lines at these points.

Figure 7 shows the radial profiles of the hysteresis width $\Delta q_{\rm e}/n_{\rm e}$. The values at the edge of the error band correspond to those at $-\nabla T_{\rm e,max}$ and $-\nabla T_{\rm e,min}$, respectively. Therefore, if the two linear fitting lines at the top side and the bottom side are completely parallel, the width of the error band becomes zero. The hysteresis width is plotted in $r_{\rm eff} > 0.13$ m, in which the ECH power absorption is almost absent. As being apart from the power absorption region, the hysteresis width decreases almost monotonically, regardless of the line averaged density. The hysteresis width converges to zero around $r_{\rm eff} \sim 0.35$ m.

The line averaged density dependence of the hysteresis width is plotted for different radii in Fig. 8 (a). As the line averaged density increases, the hysteresis width decreases. This tendency is consistent with the empirically recognized density dependence of the nonlocal transport, i.e., the lower the density becomes, the more the nonlocal transport event appears clearly. The contour of the hysteresis width is shown as a function of the radius and the line averaged density in Fig. 8 (b). In the same parameter space, the delay time is shown in Fig. 8 (c). The regions where the hysteresis width is large and where the delay time profile is nearly flat simultaneously decrease as the line averaged density increases. According to a theory [14, 15], the immediate response of the heat flux can be explained by the direct heating power absorption by long-wavelength fluctuations. From the view point of [14, 15], shrinking of the region where the hysteresis width is large can be explained by decreasing the eigen mode width of the long-wavelength mode. It is also natural to consider that the fast propagation of the heat pulse, i.e., the flattening

of the delay time profile, is also due to the long-wavelength fluctuation.

4. Discussion

In the theoretical model shown in [14, 15], it is predicted that the change in the heating power directly affects the fluctuation amplitude and transport. When the heating absorption is dependent on plasma parameters, e.g., the electron pressure in the model, fluctuations in the plasma parameter alter the heating absorption. The original fluctuations in the plasma parameter can be amplified by the fluctuations in the heating power absorption, which acts as a new destabilizing mechanism. The fluctuation amplitude at the saturation level is predicted as

$$I = \frac{I_0}{1 - \gamma_{\rm h} \chi_0^{-1} k_\perp^{-2}}, \tag{3}$$

where χ_0 is the turbulent diffusivity, $k_\perp$ is the wavenumber of fluctuations that are of interest, and

$$\gamma_{\rm h} \equiv \frac{\partial P_{\rm ECH}}{\partial p_{\rm e}} \tag{4}$$

is the magnitude of the direct influence of the heating source on the fluctuation amplitude. The fluctuation amplitude without the direct heating effect I_0 is amplified to I when the denominator in the r.h.s. is smaller than unity. The time scale of the change of the fluctuation amplitude can be much faster than that of the fluctuation growth only with the local effect.

In the literature [21], a model of the ECH absorption is given as a function of the electron density and the electron temperature. Here, we directly evaluate the

term $\gamma_{\rm h}\chi_0^{-1}k_\perp^{-2}$ based on the formulae in [21] and discuss whether Eq. (3) explains the experimental observation. Figure 9 (a) shows the electron density and the electron temperature dependence of the fractional power absorbed by the plasma,

$$A(n_{\rm e}, T_{\rm e}) = 1 - \exp(-\eta), \tag{5}$$

where η is the dimensionless optical depth. Here, the incident angle of the ray is treated as a fixed parameter and is obtained from the results of the ray-tracing code. The flection of the ray is small because of the relatively low electron density. Figure 9 (b) is the electron pressure derivative of the absorption power,

$$\gamma_{\rm h} = \frac{dP_{\rm ECH}}{dp_{\rm e}} = \frac{P_{\rm ECH}(r_{\rm eff})}{p_{\rm e}}\left(n_{\rm e}\frac{\partial A}{\partial n_{\rm e}} + T_{\rm e}\frac{\partial A}{\partial T_{\rm e}}\right). \tag{6}$$

This equation means that the turbulence amplification $\gamma_{\rm h}$ increases when a larger heating power is applied or the parameter derivative of the absorption rate is large. This work examine the latter point, while the previous work [3] has proven the former. At a fixed temperature, decreasing density increases $\partial P_{\rm ECH}/\partial p_{\rm e}$ so that the hystereses in the fluctuation amplitude and the transport are expected to be enhanced, which is not in contradiction with the present observation. The model is qualitatively examined by evaluating the largest possible magnitude of the hysteresis in the fluctuation amplitude with the parameters $k_\perp = m/r \sim 5$ m^{-1} for $m = 1$ global fluctuation and $\chi_0 = 1$ m^2/s [22]. The trajectory of $(n_{\rm e}, T_{\rm e})$ in $0.2 < r_{\rm eff} < 0.3$ m where the hysteresis width is large is plotted in Fig. 9 (b) for # 138118. The value is $\partial P_{\rm ECH}/\partial p_{\rm e} \sim 1$ s^{-1} that gives $\gamma_{\rm h}\chi_0^{-1}k_\perp^{-2} \sim O(0.1)$. Therefore, the long wavelength oscillation can be amplified by the ECH application.

It should be noted that the hysteresis width in the electron heat flux obtained in previous section is used as a proxy of the turbulence amplification, since no systematic turbulence measurement has been performed in the target discharges. Previous work [3] showed that the hysteresis width in the electron heat flux is nearly proportional to that in the turbulence amplitude. In the higher density case, $\partial P_{\mathrm{ECH}}/\partial p_{\mathrm{e}}$ is much smaller than unity that makes $\gamma_{\mathrm{h}}\chi_0^{-1}k_\perp^{-2} \sim 0$, therefore the model predicts no hysteresis. However, the finite hysteresis response is observed in a wider range of the electron density including the higher electron density range. Although the estimation of χ_0 may not be accurate enough, the model tends to estimate the parameter window in which the hysteresis emerges narrower than the experimental observation. The limitation of the predictive capability of the present model may come from several simplifications for the analytical transparency, as discussed in [14, 15]. Further model development as well as the direct observation of the response in the fluctuation amplitude are desirable for achieving more quantitative understanding.

Recently, the relation between the nonlocality of the electron thermal transport and the confinement power degradation was discussed in the TJ-II stellarator [23]. It was concluded that the more the input power is increased the larger the nonlocality of transport becomes, which leads to a significant power degradation of confinement. Existence of the transport hysteresis is highly related to the fast propagation of heat pulse that was observed in [23]. Inspired by their view, study of the power degradation using the transport hysteresis analysis would be an interesting issue for future work.

5. Summary

In this paper, we performed analysis of the density scan experiment in order to clarify how the hysteresis width depends on the density. As the line averaged density increases, the hysteresis width almost monotonically decreases. To discuss the physical mechanism of the hysteresis formation, a theoretical model describing the direct response of the fluctuation amplitude to the heating was examined. The model predicts that decreasing density enhances the hysteresis width in the turbulent thermal transport, which was not in contradiction with the present observation. It was found that the model tends to estimate the parameter window in which the hysteresis emerges narrower than the experimental observation, showing the necessity of further model development as well as direct observation of the response in the fluctuation amplitude.

Appendix

In the analysis of the electron heat flux using the energy conservation equation, uncertainty in the evaluation of the ECH absorption profile is directly reflected in the results. It is essential to examine whether the observed hysteresis can be explained by the error of the antenna position. In the ECH system in the LHD, the ECH injection angle is controlled by the two-dimensional steering antenna manipulator. Here, we reproduce the ECH absorption profiles with the largest possible errors of incident angle in the horizontal directions and the vertical directions. Considering the manipulator resolution, the errors of angle in the horizontal direction $\sim \pm 0.46^\circ$ and the vertical

direction $\sim \pm 0.48^\circ$ are added to the setting incident angle. The combination of errors in the horizontal direction and in the vertical direction give 9 different ECH absorption profiles, as plotted in Fig. 10. All the absorption profiles have their peak in $r_{\rm eff} < 0.15$ m.

The ECH absorption profile that makes the hysteresis width zero can also be calculated from the time evolution of the electron temperature perturbation, and is shown by the green curve in Fig. 10. In the insert, the reevaluated hysteresis width profile is shown by green curve in addition to the $\Delta q_{\rm e}$ profile. The absorption profile that makes the hysteresis width zero has two peaks at the center and $r_{\rm eff} \sim 0.2$ m. To explain the finite hysteresis width by only the misestimation of the ECH absorption profile, an unreasonable error in the steering antenna setting must be introduced, which can be excluded.

Acknowledgments

The authors acknowledge all the members of the LHD Experiment Group for their assistance. The authors also thank Professors S. Sakakibara, K. Tanaka, S. Kubo, and T. Shimozuma for strong support and useful discussions. This work is partly supported by the National Institute for Fusion Science grant administrative budget (ULHH033) and the Grant-in-Aid for Scientific Research of JSPS (17K14898, 15H02155, and 16H02442).

References

[1] U Stroth, L Giannone, H J Hartfuss, *et al* 1996 *Plasma Phys. Control. Fusion* **38** 611

[2] K W Gentle, M E Austin, J C DeBoo, T C Luce, and C C Petty 2006 *Phys. Plasmas* **13** 012311

[3] S Inagaki, T Tokuzawa, N Tamura, S-I Itoh, T Kobayashi, K Ida, T Shimozuma, S Kubo, K Tanaka, T Ido, *et al* 2013 *Nucl. Fusion* **53** 113006

[4] J D Callen and G L Jahns 1977 *Phys. Rev. Lett.* **38** 491

[5] E D Fredrickson, K McGuire, A Cavallo, R Budny, A Janos, D Monticello, Y Nagayama, W Park, G Taylor, and M C Zarnstorff 1990 *Phys. Rev. Lett.* **65** 2869–2872

[6] M W Kissick, E D Fredrickson, J D Callen, C E Bush, Z. Chang, P C Efthimion, R A Hulse, D K Mansfield, H K Park, J F Schivell, *et al* 1994 *Nucl. Fusion* **34** 349

[7] K W Gentle, W L Rowan, R V Bravenec, G Cima, T P Crowley, H Gasquet, G A Hallock, J Heard, A Ouroua, P E Phillips, D W Ross, P M Schoch, and C Watts 1995 *Phys. Rev. Lett.* **74** 3620–3623

[8] N Tamura, S Inagaki, K Tanaka, C Michael, T Tokuzawa, T Shimozuma, S Kubo, R Sakamoto, K Ida, K Itoh, *et al* 2007 *Nucl. Fusion* **47** 449

[9] K Ida, Z Shi, HJ Sun, S Inagaki, K Kamiya, JE Rice, N Tamura, PH Diamond, G Dif-Pradalier, XL Zou, *et al* 2015 *Nucl. Fusion* **55** 013022

[10] K Itoh, S-I Itoh, K Ida, S Inagaki, Y Kamada, K Kamiya, JQ Dong, C Hidalgo, T Evans, WH Ko, *et al* 2017 *Nucl. Fusion* **57** 102021

[11] S Inagaki, S-I Itoh, K Itoh, N Kasuya, T Kobayashi, A Fujisawa, T Tokuzawa, K Ida, S Kubo, T Shimozuma, *et al* 2013 *Plasma Fusion Res.* **8** 1202173

[12] S Inagaki, S-I Itoh, K Itoh, K Ida, D López-Bruna, M A Ochand, T Estrada, B Ph van Milligen, C Hidalgo, and N Kasuya 2014 *Plasma Fusion Res.* **9** 1202052

[13] T Kobayashi, K Ida, S Inagaki, H Tsuchiya, N Tamura, GH Choe, GS Yun, HK Park, WH Ko, TE Evans, *et al* 2017 *Nucl. Fusion* **57** 076013

[14] S-I Itoh and K Itoh 2012 *Sci. Rep.* **2** 860

[15] S-I Itoh and K Itoh 2013 *Nucl. Fusion* **53** 073035

[16] H Tsuchiya, Y Nagayama, K Kawahata, S Inagaki, S Kubo, *et al* 2011 *Plasma Fusion Res.* **6** 2402114–2402114

[17] T Ii Tsujimura, S Kubo, H Takahashi, R Makino, R Seki, Y Yoshimura, H Igami, T Shimozuma, K Ida, C Suzuki, *et al* 2015 *Nucl. Fusion* **55** 123019

[18] K Ida, S Inagaki, T Shimozuma, N Tamura, H Funaba, K Narihara, S Kubo, S Murakami, A Wakasa, M Yokoyama, *et al* 2004 *Phys. Plasmas* **11** 2551–2557

[19] T Kobayashi, K Itoh, K Ida, S Inagaki, and S-I Itoh 2017 *J. Phys. Soc. Jpn.* **86** 074501

[20] K Ida, S Inagaki, Y Suzuki, S Sakakibara, T Kobayashi, K Itoh, H Tsuchiya, C Suzuki, M Yoshinuma, Y Narushima, *et al* 2013 *New J. Phys.* **15** 013061

[21] A C England, O C Eldridge, S F Knowlton, M Porkolab, and J R Wilson 1989 *Nucl. Fusion* **29** 1527

[22] H Funaba, K Watanabe, S Sakakibara, I Yamada, K Tanaka, T Tokuzawa, M Osakabe, Y Narushima, N Nakajima, M Yokoyama, *et al* 2007 *Fusion Sci. Tech.* **51** 129–137

[23] B Ph van Milligen, B A Carreras, C Hidalgo, Á Cappa, and TJ-II team 2018 *Phys. Plasmas* **25** 062503

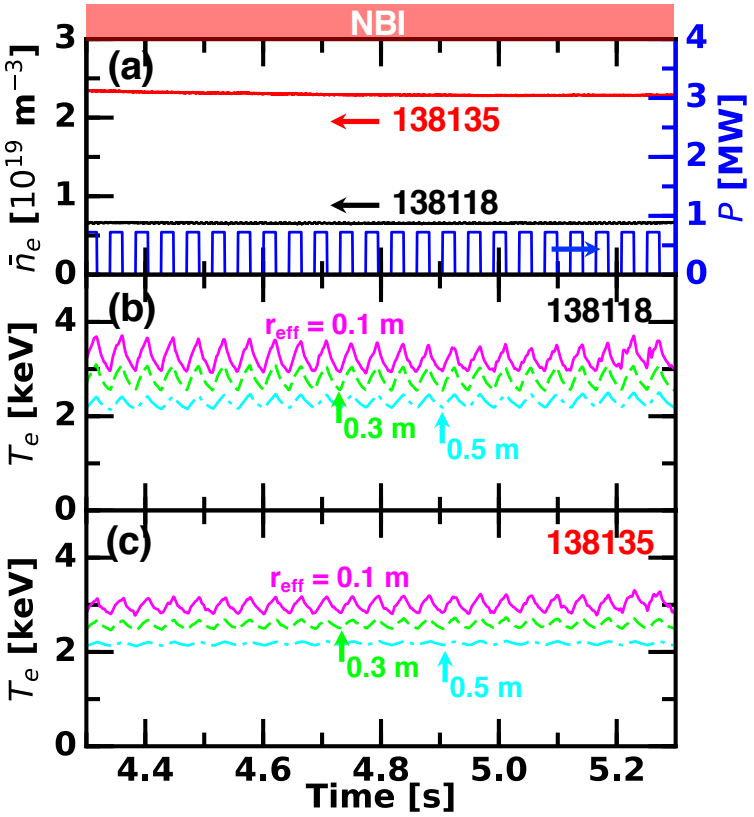

Figure 1. Time evolutions of (a) the line averaged density and the ECH port through power and the electron temperature, (b) of the lower density discharge (#138118), and (c) of the higher density discharge (#138135). The MECH pulse pattern is identical for all the discharges.

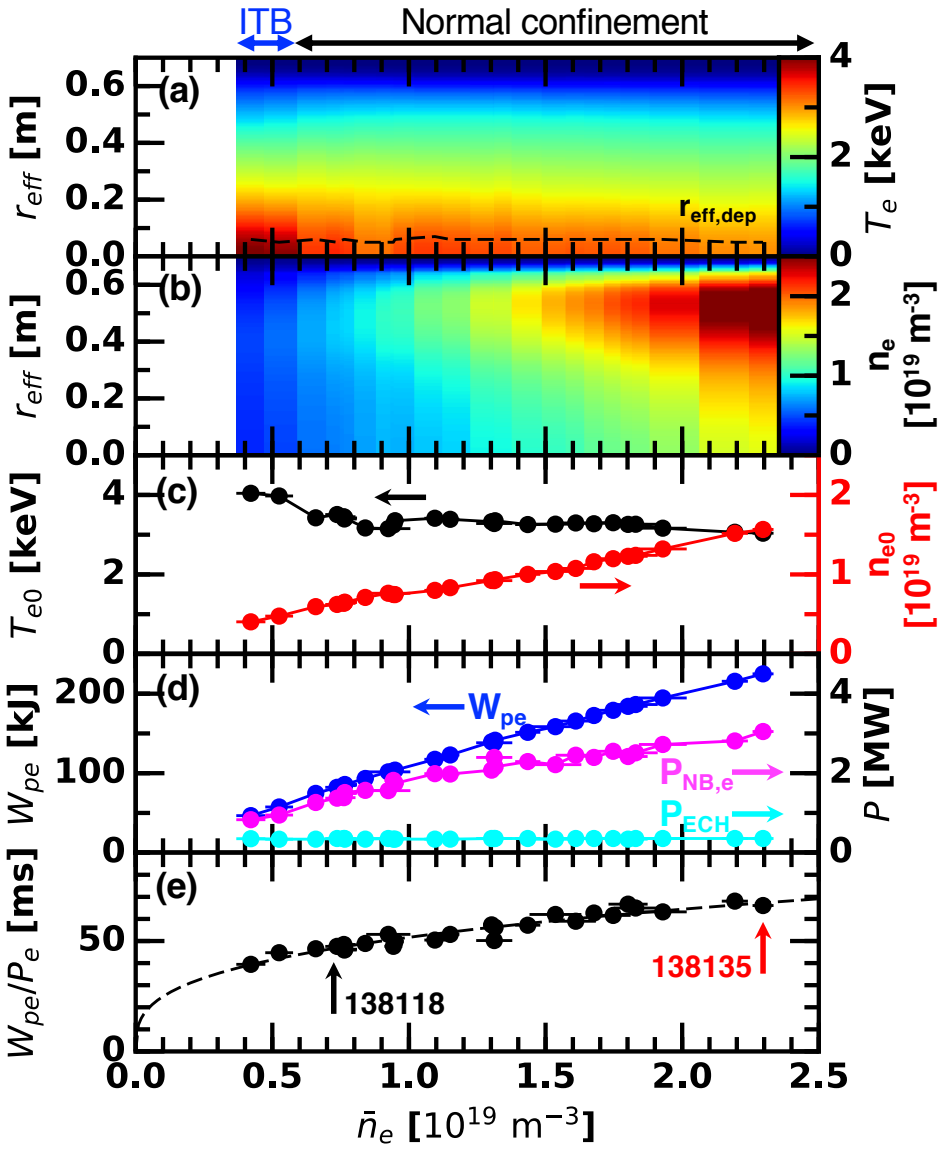

Figure 2. The line averaged density dependence of (a) the electron temperature profile, (b) the electron density profile, (c) the electron temperature and the electron density at the plasma center, (d) the plasma stored energy by electrons and the plasma heating power for electrons by the ECH and by the NBI, and (e) the plasma stored energy by electrons divided by the total heating power for electrons.

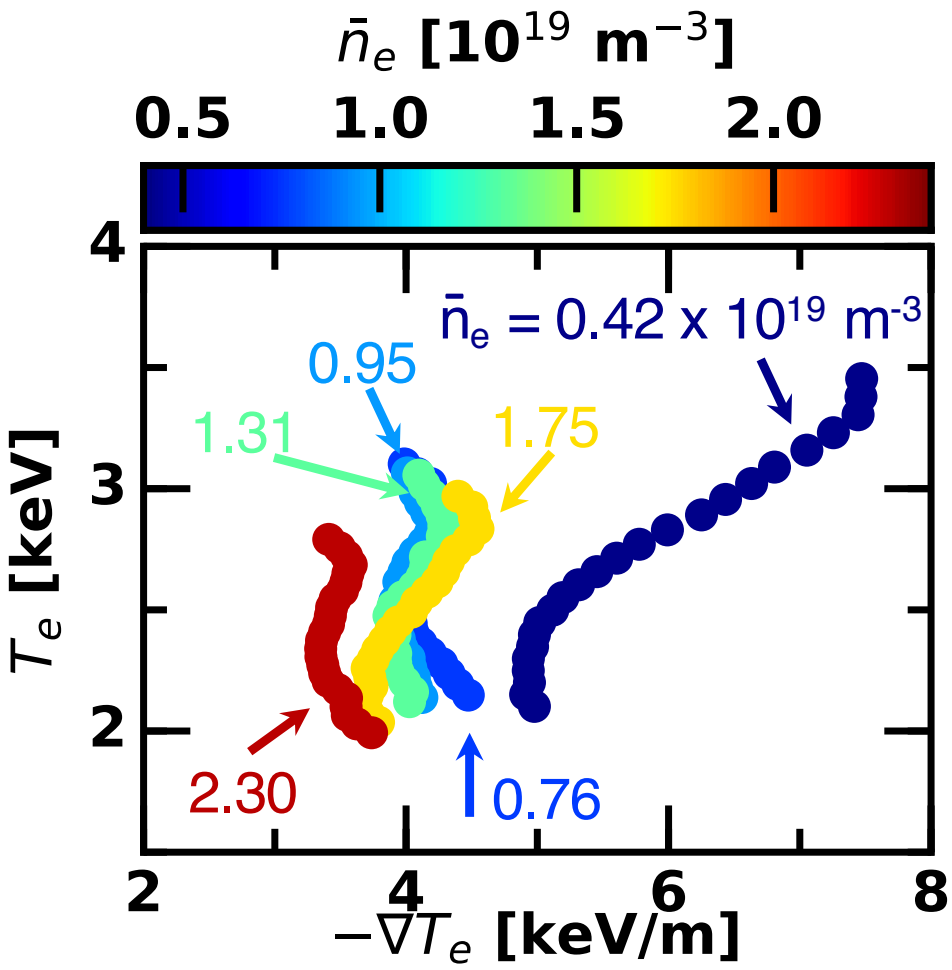

Figure 3. The electron temperature plotted as a function of the electron temperature gradient in $0.12 \leq r_{\rm eff} \leq 0.35$ m. Different colors of symbols show the line averaged density of the discharge.

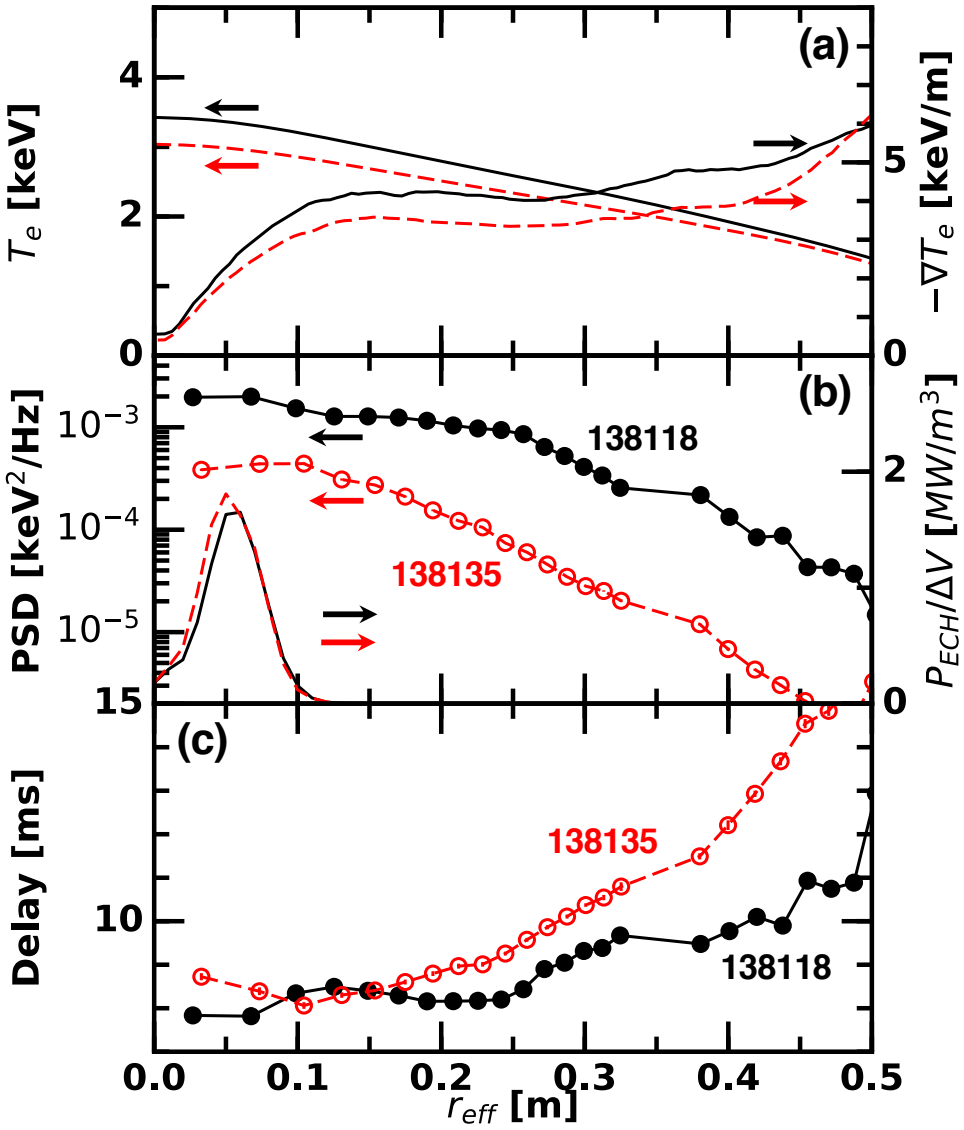

Figure 4. Radial profiles of (a) the electron temperature and the electron temperature gradient, (b) the power spectral density of the electron temperature perturbation at the MECH frequency and the MECH absorption power density, and (c) the time delay of the electron temperature perturbation with respect to the MECH pulse for the lower density discharge (#138118) and the higher density discharge (#138135).

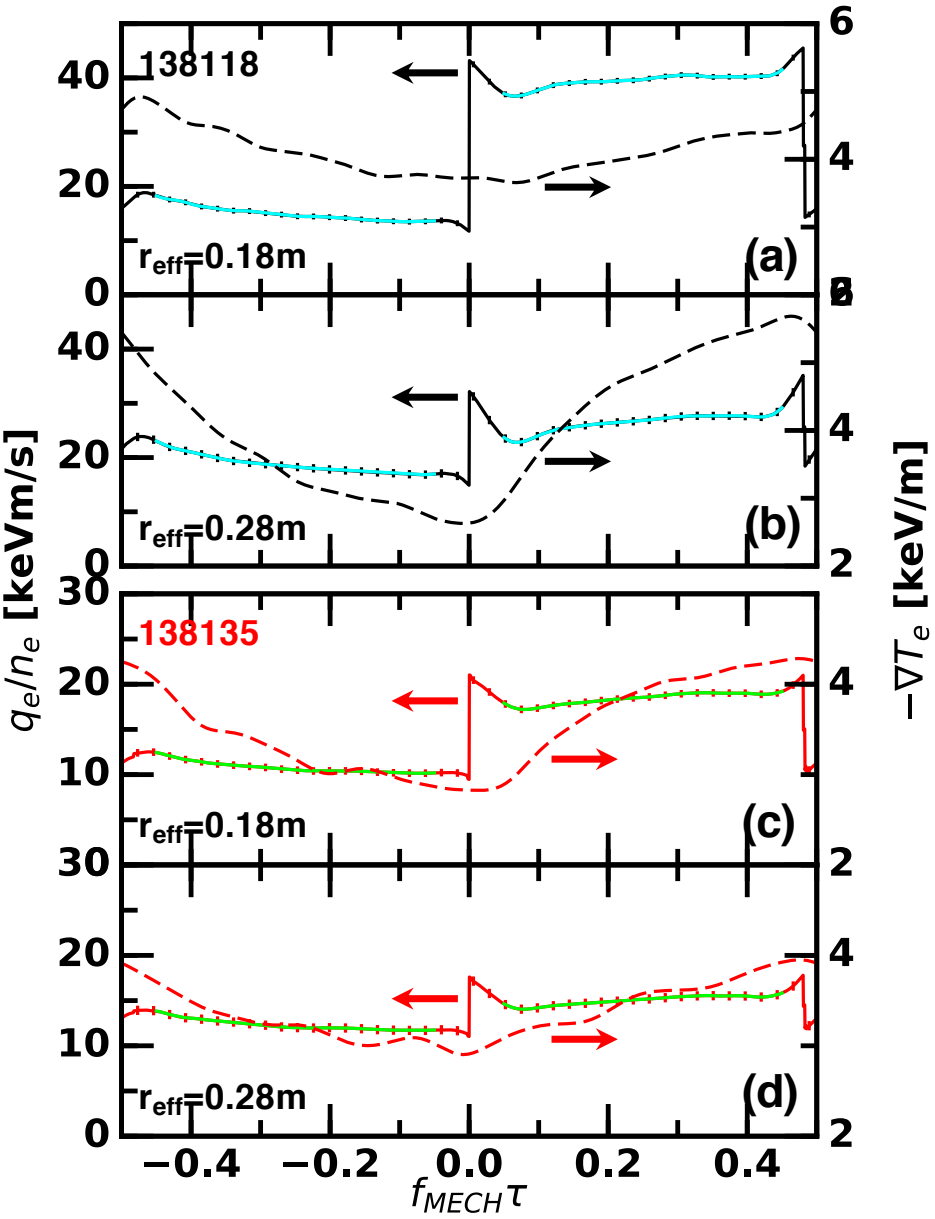

Figure 5. Time evolutions of the heat flux and the electron temperature gradient at $r_{\rm eff} = 0.18$ m [(a,c)] and at $r_{\rm eff} = 0.28$ m [(b,d)] for the lower density discharge (#138118, two panels at the top) and the higher density discharge (#138135, two panels at the bottom). Light blue lines (light green lines) in top (bottom) two figures show the data used for evaluating the hysteresis width.

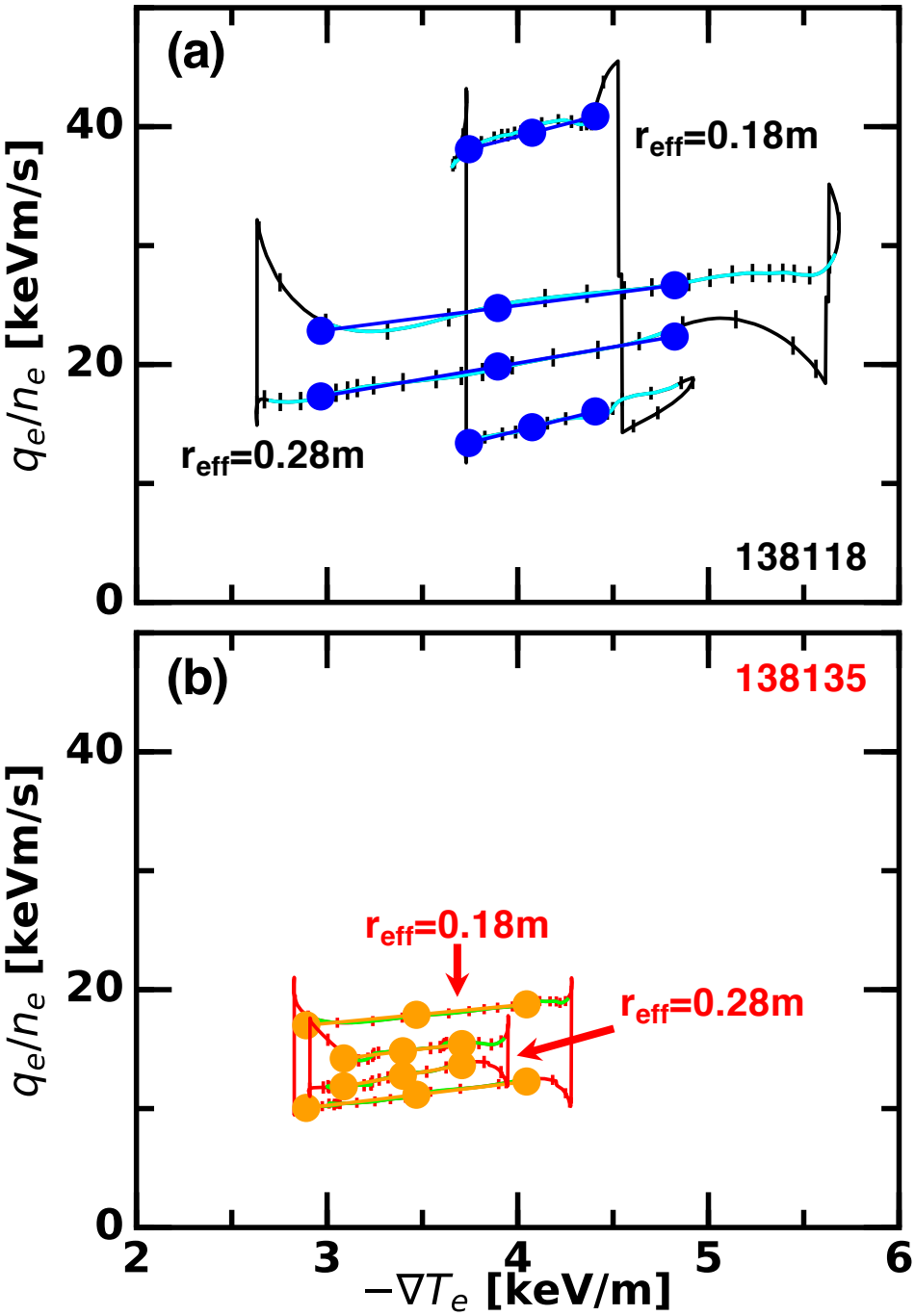

Figure 6. Diagrams of the flux gradient relation for (a) the lower density discharge (#138118) and (b) the higher density discharge (#138135).

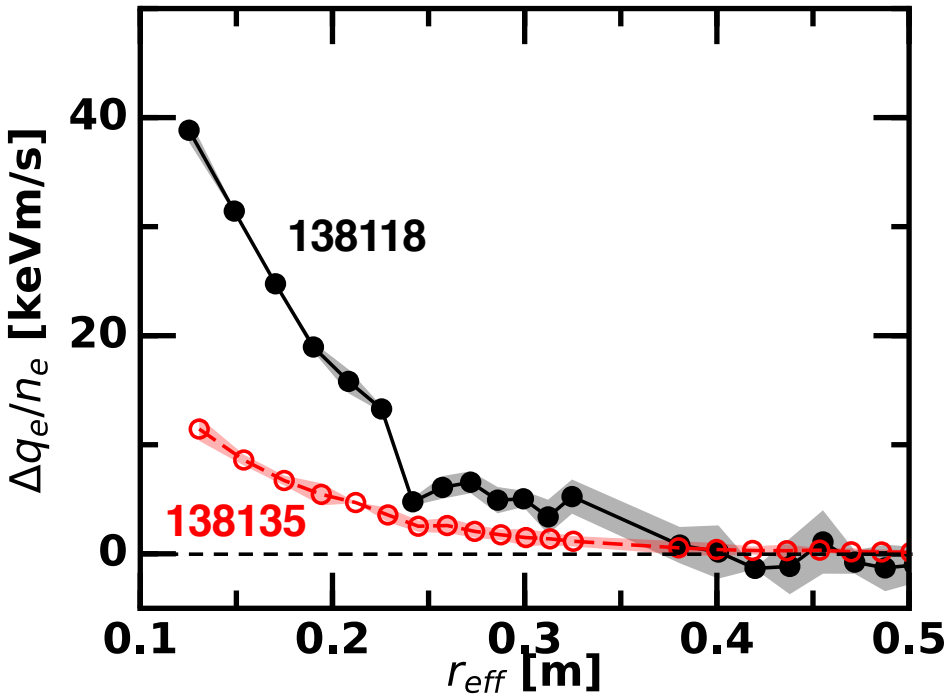

Figure 7. Radial profile of the width of the hysteresis in the flux-gradient relation for the lower density discharge (#138118) and the higher density discharge (#138135).

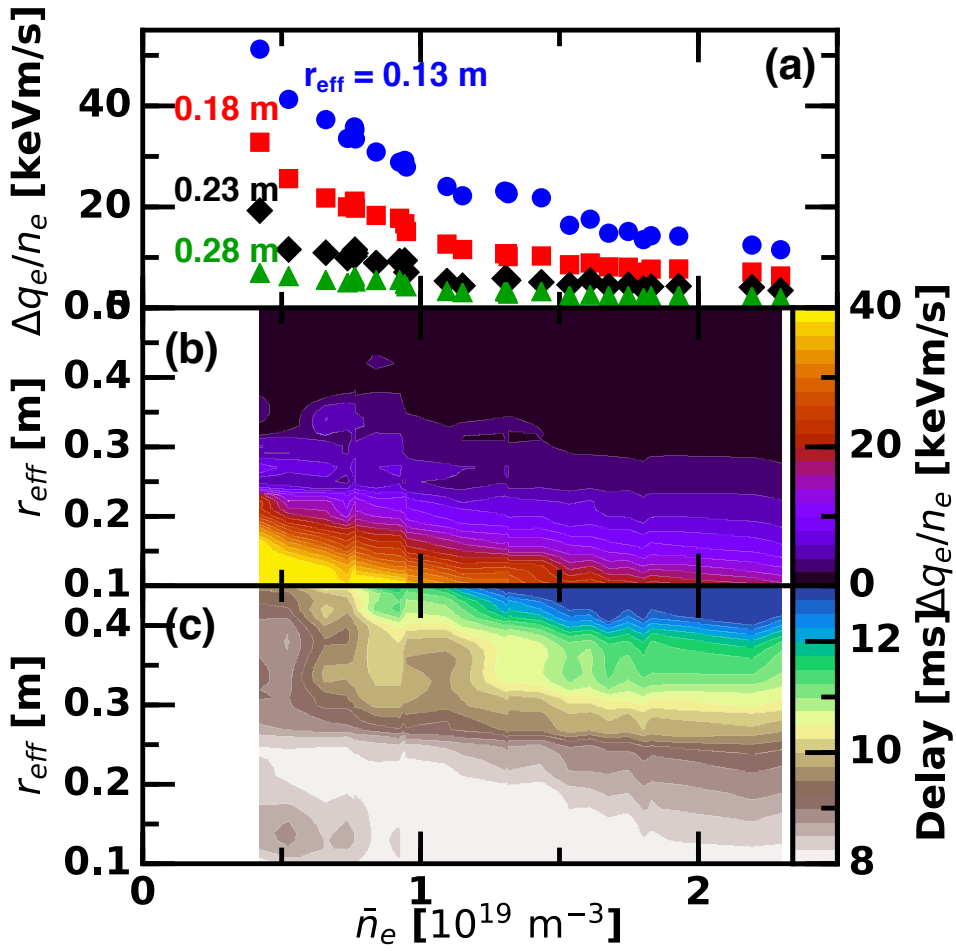

Figure 8. The line averaged density dependence of (a) the width of the hysteresis at the different radii, (b) the radial profile of the width of the hysteresis, and (c) the radial profile of the time delay of the temperature perturbation.

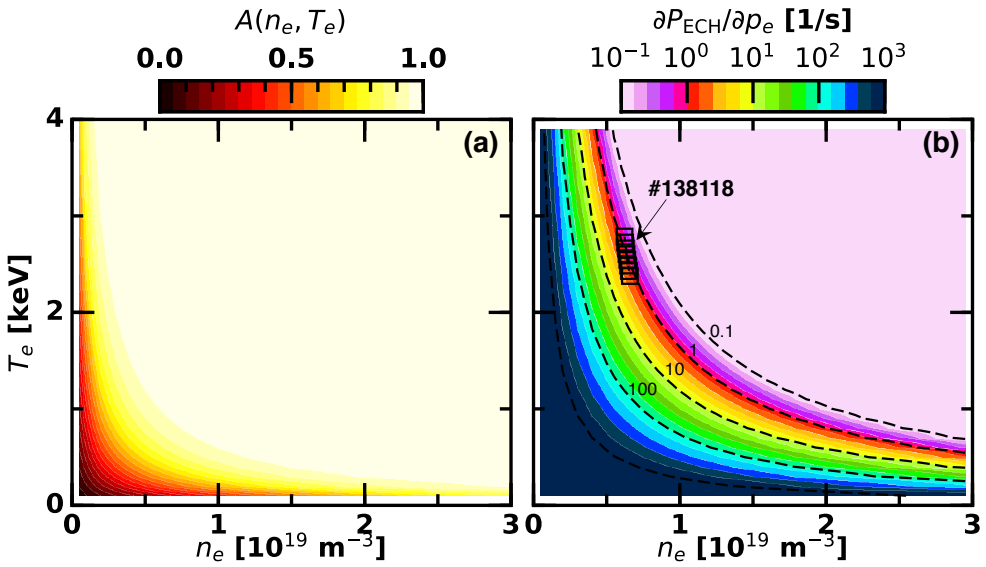

Figure 9. The electron temperature and the electron density dependences of (a) the ECH absorption efficiency and (b) the electron pressure derivative of the ECH absorption power.

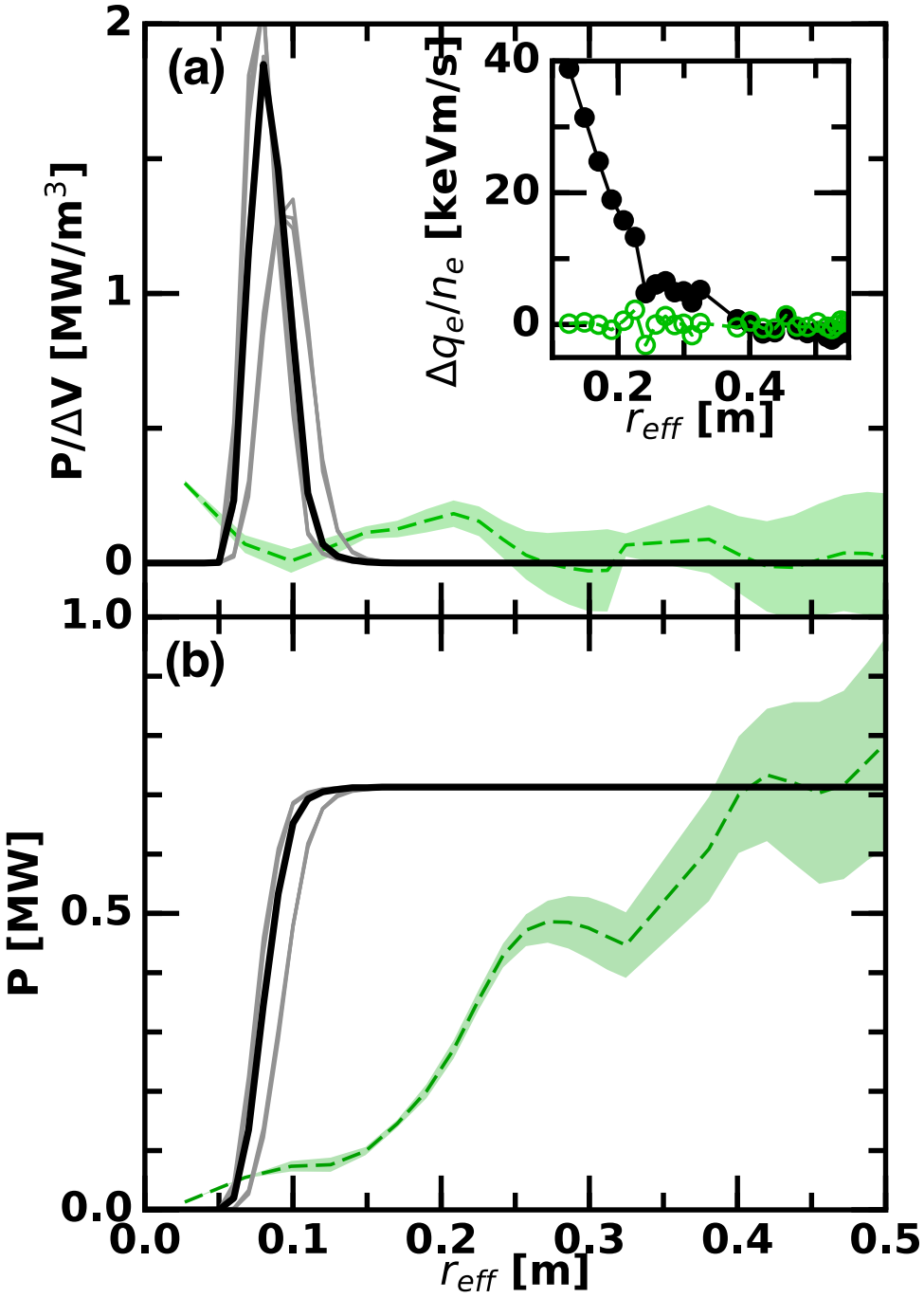

Figure 10. Radial profiles of (a) the MECH absorption power density and (b) the volume integrated total absorption power. (Black thick) Absorption profile calculated by the ray-trace code. (Gray) Possible errors of the steering antenna angle in different directions. (Green dashed) Calculated absorption profile that makes the hysteresis width zero. (Insert) Radial profiles of the hysteresis width obtained with the MECH absorption profile shown by black curve and green curve, respectively.